# ACOUSTIC END CORRECTION IN MICRO-PERFORATED PLATES - REVISITED

Muttalip Aşkın Temiz, Ines Lopez Arteaga

*Eindhoven University of Technology, Dept. of Mechanical Engineering, Eindhoven, The Netherlands,*
*e-mail: m.a.temiz@tue.nl*

Gunilla Efraimsson, Mats Åbom

*KTH Royal Institute of Technology, Dept. of Aeronautical and Vehicle Engineering, Stockholm, Sweden,*

and Avraham Hirschberg

*Eindhoven University of Technology, Dept. of Applied Physics, Eindhoven, The Netherlands,*

Micro-Perforated plates (MPP) are plates with a porosity of the order of 1% in which the perforation diameter is optimized for absorption of incident acoustic waves. The concept has been introduced by Maa[1], who proposed an analytical model based on the solution for the oscillating viscous flow in a long capillary tube. The finite length of the geometry is taken into account by reactive and resistive end-corrections of Ingard[2]. In order to match experimental data, the single sided resistive end correction of Ingard has been multiplied by a factor $\alpha$. This factor varies in the literature in the range $2 \leq \alpha \leq 4$. Bolton and Kim[3] propose the use of CFD to determine these end-corrections. Using a similar approach, our present work proposes an alternative result to their work. We use a linear numerical model based on incompressible Navier-Stokes equations in 2D-axisymmetric coordinates, which is solved in the Fourier domain, rather than the time domain simulation as proposed by Bolton and Kim. Working in the Fourier domain with linearized equations ensures the numerical efficiency and absence of non-linear effects. We furthermore use an alternative procedure to determine the inertial part of the transfer impedance leading to a difference of the order of 10% with the results of Bolton and Kim. Moreover, our results show that resistive and reactive end corrections are mainly a function of the Shear number $Sh$. The porosity $\sigma$ and plate thickness to perforation diameter ratio $t^*$ seems to be less important.

## 1. Introduction

Micro Perforated Plates (MPP) are plates with a porosity of the order of 1% and mostly made of metal. Supported with a back cavity, they have been used for sound absorption in room acoustics since the 70s. Although existed for more than 40 years, the absorption mechanisms of the MPPs has not been explained in detail until the study of Maa[1]. Maa combined Kirkhhoff's[5] theory for sound propagation in circular perforations with Morse and Ingard's[2, 8] end-corrections in order to model the acoustic behaviour of a finite-length perforation analytically.

Although Maa's study explains the physics behind the acoustic behaviour of MPP, some comparisons between experimental and analytical results - such as Allam and Åbom[4] - state that the end-correction coefficients, in particular the resistive part, may vary from experiment to experiment.

Based on this observation, Bolton and Kim[3] proposed a more general definition for the resistive end-correction coefficient, $\alpha$, for a MPP. In order to do that they perform a parametric study on plate thickness, $t_p$; porosity, $\sigma$; and perforation diameter, $d_p$, throughout some certain frequency span using CFD simulations. Despite the fact that their work is novel, there are some inconsistencies with the proposed numerical fit for $\alpha$.

In this study, we assume that the perforations of the plate are far enough from each other due to a low porosity, such that the perforations do not interfere. Hence, we investigate only one single perforation in order to model the whole MPP. The numerical results are validated by experiments and employing non-dimensional parameters, numerical fits for both resistive and reactive end-correction coefficients, $\alpha$ and $\delta$ respectively, are re-defined for the perfect sharp-edge limit case.

## 2. Governing Physics

The transfer impedance of a MPP is defined as:

$$Z_t = \frac{\hat{P}_1 - \hat{P}_2}{\sigma \hat{U}_p}, \tag{1}$$

where $\hat{P}_1 - \hat{P}_2$ is the plane wave pressure difference across the plate, $\sigma$ is the porosity and $\hat{U}_p$ is the volume flow divided by the perforation area. When $\hat{U}_p$ is multiplied with $\sigma$, we get plane wave normal velocity before (or after) the plate.

In case of circular perforation, the transfer impedance of a MPP with a finite plate thickness is defined by Maa[1] as follows:

$$Z_t = j\omega t_p \rho_0 \left[ 1 - \frac{2}{Sh\sqrt{-j}} \frac{J_1(Sh\sqrt{-j})}{J_0(Sh\sqrt{-j})} \right]^{-1} + 2\alpha R_S + j\delta\omega\rho_0 \frac{d_p}{2}. \tag{2}$$

The first term in the RHS of the expression in Eq. 2 models the oscillating fluid flow only within the perforation where $\omega = 2\pi f$ is the radial frequency, $t_p$ is plate thickness, $\rho_0$ is the density of air, $j$ is the imaginary number $\sqrt{-1}$, $J_n$ is the 1st kind of Bessel function of order $n$ and $Sh$ is the Shear number which is defined[6] as $Sh = d_p\sqrt{\omega\rho_0/(4\mu)}$ where $d_p$ is the perforation diameter and $\mu$ is the dynamic viscosity of air.

The end effects become very important in plates with normalized thickness, $t^* = t_p/d_p$, in the order of unity. Therefore, in Eq. 2, the second term in RHS is the resistive and the last one is the reactive (inertial) end-correction expression, respectively, where $R_S$ is the surface resistance on one side of the plate and calculated by $R_S = 0.5\sqrt{2\mu\rho_0\omega}$. Although resistive and reactive end-correction coefficients are defined by Ingard[2] as $\alpha = 2$ and $\delta = 1.64$; as mentioned before, it is observed in the literature that different experiment set-ups require different end-correction constants to match the theoretical with the experimental results. For example, Allam and Åbom[4] propose $\alpha = 4$ for sharp edges and $\alpha = 2$ for round edges.

In the numerical solutions of the Reynolds averaged non-linear Navier-Stokes (RANS) equations by Bolton and Kim, a viscous, incompressible oscillating flow in time domain for a 2D axisymmetric geometry of a single perforation is studied. Likewise, in this paper a viscous, incompressible flow is considered. However, we employ linearized Navier-Stokes equations in Fourier domain. Another important difference is in the determination of the pressure difference along the micro-perforation, as we will describe further.

With this study, we suggest a revised definition for $\alpha$ and $\delta$ investigating the effect of Shear number, $Sh$.

## 3.  Numerical Model

A single micro-perforation is simulated numerically using a finite element model in COMSOL Multiphysics® v4.3b in order to calculate transfer impedance, $Z_t$, of a MPP. The 2-D axisymmetric computational domain is shown in Fig. 1.
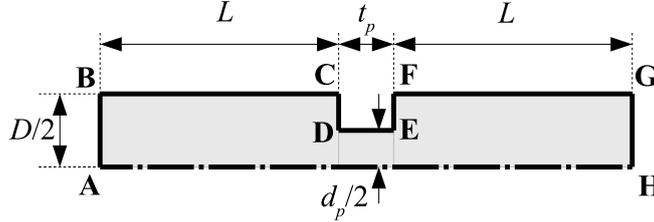


Figure 1: Computational domain of a single perforation.

As can be seen from Fig. 1, the computational domain covers regions inside as well as outside the perforation. As a result, the diameter of the upstream / downstream fluid is calculated as $D = d_p/\sqrt{\sigma}$. The upstream and downstream length of the model is designed as $L = 3D$ in order to make sure that the effect of the perforation on the flow is negligible at the inlet and outlet boundaries.

The transfer impedance of the single perforation is defined by considering the acoustic pressure difference between the two sides of the perforation and dividing this by the volume flux per surface area passing through the perforation as stated in Eq. 1. The relevant acoustic pressure at one side of the perforation is obtained by linear extrapolation, assuming an incompressible uniform flow, from the inlet (or the outlet) boundary of the computational domain to the surface of the perforation. In our numerical model the pressure difference $(\hat{P}_1 - \hat{P}_2)$ is therefore given by

$$\hat{P}_1 - \hat{P}_2 = \hat{P}_u - \hat{P}_d - j2L\rho_0\omega\hat{U}, \tag{3}$$

where $\hat{P}_u$ and $\hat{P}_d$ are the upstream and downstream pressures at the inlet and outlet of the numerical domain respectively and $\hat{U}$ is the imposed uniform inlet velocity of the model. The boundary conditions are: $|AB|$ harmonic velocity inlet; $|BC|$ and $|FG|$ slip wall; $|CD|$, $|DE|$ and $|EF|$ no-slip wall; $|GH|$ viscous free, zero pressure outlet and $|AH|$ radial symmetry axis.

For the mesh generation, COMSOL Multiphysics®'s built-in physics controlled mesh generating tool is used. The difference in the calculated impedance between two successive grid levels is less than 0.02%. In order to avoid the numerical singularity caused by sharp edges, tiny fillets are created in the model. Simulations for three different values of the ratio of the radius of the fillet, $r_f$, to the hole diameter, $d_p$, namely $6.25 \times 10^{-3}$, $3.13 \times 10^{-3}$ and $1.56 \times 10^{-3}$ are conducted. The changes in the calculated impedance are observed to be proportional to $r_f/d_p$, hence the sharp-edge $r_f/d_p = 0$ limit is estimated by linear extrapolation.

## 4.  Experiment Model

### 4.1  Experiment method and Accuracy

In order to verify the numerical simulation results, 3 MPP samples are studied experimentally. The samples are made of brass plates and the perforations of diameter $d_p$ are obtained by drilling. All 3 samples have similar porosity $\sigma = (0.74 \pm 0.02)\%$. Table 1 shows their geometrical specifications.

Samples defined in Table 1 have circular geometry with a diameter of $5\ cm$. They are placed between flanks with O-rings at the end of the impedance tube. The tube is $1\ m$ long and has six *BSWA MPA416* microphones with the sensitivity of $50.45\ mV/Pa$. They are equally distributed with a distance of $175\ mm$. The microphones are relatively calibrated for the frequency range of $100\ Hz$ to $700\ Hz$. LabView® is used for data acquisition and a Matlab® script with a lock-in method is used

Table 1: Sample specifications.

| Sample | $t_p\ [mm]$ | $d_h\ [mm]$ |
|--------|-------------|-------------|
| A | $1.0 \pm 0.01$ | $0.3 \pm 0.05$ |
| B | $1.0 \pm 0.01$ | $0.8 \pm 0.05$ |
| C | $1.6 \pm 0.01$ | $1.6 \pm 0.05$ |

for post-processing. A loudspeaker closes the tube end opposite to the sample. This loudspeaker is driven by a harmonic signal of frequency $f$. Due to thermo-acoustic effects, a temperature gradient will be induced by acoustical forcing for some time. The system runs 10 seconds for each frequency and in post-processing, the first and last 3 seconds are omitted in order to get rid of the transient effects.

The measurements are affected by the speed of sound within the tube. After 20 steps in the frequency, we wait 15 minutes in order to restore the uniform temperature in the tube. The plane wave decomposition in the tube is obtained by a least square fit of the 6 microphone signals. For 20 frequency steps we have 40 wave amplitudes as unknown plus the speed of sound, $c_0$, as additional unknown. The signals of the 6 microphones provide a set of 120 equations for those 41 unknowns, which is solved by least square[9]. For the completely closed-end case, the deviation of the measured reflection coefficient is less than 0.1% from the theoretical case.

We measur the transfer impedance employing the following procedure:

i. Measure the open end reflection coefficient of the open impedance tube without the plate, $R_{OE}$, and calculate the radiation impedance, $Z_R$, using $Z_R = \rho_0 c_0 (1 + R_{OE})/(1 - R_{OE})$.

ii. Fix the MPP sample to the end, measure the reflection coefficient of sample-loaded end, $R_P$, and calculate $Z_P = \rho_0 c_0 (1 + R_P)/(1 - R_P)$.

iii. Obtain the transfer impedance of the plate, $Z_t$, by subtracting the radiation impedance from the sample-loaded end impedance: $Z_t = Z_P - Z_R$.

During experiments, we observe a spurious local reflection peak around $300 Hz$ in every measurement. We suspect it might be due to a mechanical vibration resonance frequency of the impedance tube. Hence, results from $250 Hz$ to $350 Hz$ are excluded throughout the study.

### 4.2 Non-linearity considerations

The Strouhal number, $Sr$, is defined as the ratio of micro-perforation diameter and fluid particle displacement $|\hat{U}|/(\sigma \omega)$ within the perforation[10]:

$$Sr = \sigma \omega d_p / |\hat{U}| \tag{4}$$

If $Sr < 1$, non-linear effects are observed: The measured impedance increases with increasing amplitude. In order to avoid non-linearity in experiments, we decrease the excitation amplitude gradually at the lowest frequency of interest, namely $100\ Hz$. When two successive measurements with different amplitudes result in the same reflection coefficient, we continue experiments at other frequencies with that particular amplitude. After the measurements, the Strouhal number is calculated in order to check the non-linearity and it is observed that $Sr$ is always larger than unity even for the lowest frequency. Hence, our measurements are certainly in the linear regime.

## 5. Numerical and Experimental Transfer Impedance Comparison

The transfer impedance values are obtained in two different ways: numerical, $Z_{t_{num}}$; and experimental, $Z_{t_{exp}}$. Real and imaginary parts of these quantities are compared in Fig. 2 separately. In order

to have simpler graphs, for each sample, the numerical and the experimental results are normalized with respect to each other. In other words, *Normalized* $\Re\{Z_t\}$ represents $\Re\{Z_{t_{num}}\}/\Re\{Z_{t_{exp}}\}$ and *Normalized* $\Im\{Z_t\}$ represents $\Im\{Z_{t_{num}}\}/\Im\{Z_{t_{exp}}\}$.
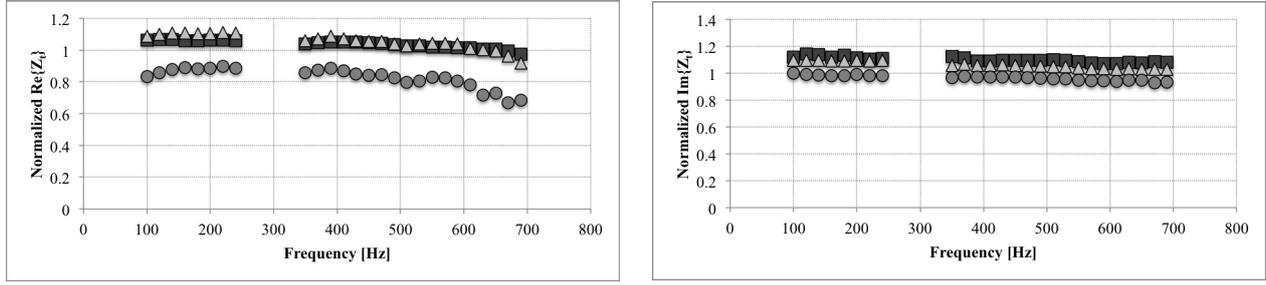


(a) Real part of the normalized transfer impedance is defined by $\Re\{Z_{t_{num}}\}/\Re\{Z_{t_{exp}}\}$

(b) Imaginary part of the normalized transfer impedance is defined by $\Im\{Z_{t_{num}}\}/\Im\{Z_{t_{exp}}\}$

Figure 2: Normalized real and imaginary parts of the transfer impedance for each sample are plotted separately: Sample A (■), Sample B (▲) and Sample C (●). Please note that the experimental data between 250 and 350 Hz are excluded.

In Fig. 2, it is clear that the value of the *Normalized* $Z_t$ is close to unity for the entire frequency range. However, some deviations of the order of 20% are evident. We expect the deviations, which are more distinctive in the resistive part, to be mainly due to uncertainties in the geometry; in particular the shape of the edges.

## 6. Calculation of Resistive and Reactive End-Correction Coefficients

With the help of Eq. 2, the resistive and the reactive end-corrections, $\alpha$ and $\delta$, can be expressed as follows:

$$\alpha = \frac{\Re\{Z_t\} - \Re\{Z_t\}_{th}}{2R_S}, \tag{5}$$

$$\delta = \frac{\Im\{Z_t\} - \Im\{Z_t\}_{th}}{\rho_0 \omega d_h/2}, \tag{6}$$

where subscript $th$ represents the word *theoretical* and calculated by the first term of on the RHS of Eq. 2. We use the numerical solutions to calculate $Z_t$ since the edge sharpness does not change between different cases in the simulations. In order to ensure the dynamic similarity, instead of using dimensional $f$, we use the non-dimensional Shear number, the porosity appears to have no effect on the results. Moreover, for $t_p/d_p = \mathcal{O}(1)$, our results indicate that $Sh$ is the only independent variable.

Figure 3 illustrates the scattering of $\alpha$ and $\delta$ with respect to $Sh$. Even for different samples, $\alpha$ and $\delta$ are almost equal for the same value of $Sh$. This indicates a high dependence on $Sh$ for both these coefficients. As a result, we use $Sh$ as the only independent variable in the determination of a fit of the end-correction coefficients.

We calculated the following fits for the resistive and reactive end-correction coefficients:

$$\alpha = -0.12/Sh^3 + 2.30/Sh^2 + 2.76/Sh + 1.48, \ 1 < Sh < 14, \tag{7}$$

$$\delta = -0.66/Sh^2 + 1.49/Sh + 1.56, \ 1 < Sh < 14. \tag{8}$$

The graphs of the fits, which are expressed in Eqs. 7 and 8, are also shown in Fig. 3. By inspection, we conclude that the suggested fits represent the behaviour of the resistive and reactive

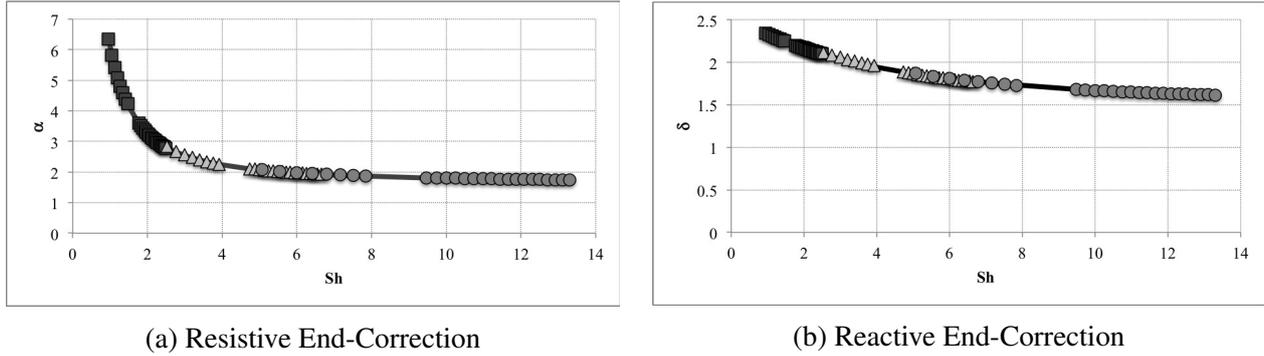(a) Resistive End-Correction



(b) Reactive End-Correction

Figure 3: Calculated numerical end corrections for all 3 samples and the fit derived from the data: Sample A (■), Sample B (▲), Sample C (●) and the fit (—).

end-corrections very well. With this fit, the fit quality $R^2$ is calculated to be 0.9986 for $\alpha$ and $\delta$ where $(1 - R^2)$ is the variance of the deviation from the data.

Whilst extrapolating to the limit case, a fillet is created with a normalized radius of $r_f/d_p = 6.25 \times 10^{-3}$ for each sample configuration. Taking the perfect sharp-edge case as the reference, real and imaginary parts of normalized transfer impedance values of the rounded edge case are calculated. From Fig. 4, one can see that a fillet with a radius of 0.6% reduces the predicted transfer impedance by 0.4% compared to the perfect sharp-edge case.



(a) Real part of normalized transfer impedance



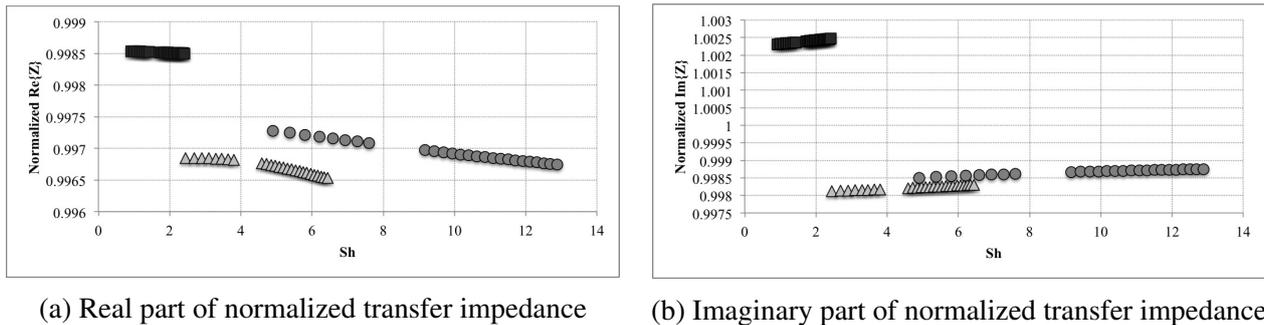(b) Imaginary part of normalized transfer impedance

Figure 4: In these graphs, we show the ratio of the calculated transfer impedance for rounded edges with $r_f/d_p = 0.6\%$ compared to the results obtained by extrapolation for $r_f/d_p = 0$: Sample A (■), Sample B (▲), Sample C (●).

## 7. Discussions and Conclusions

We perform numerical simulations of the solutions to the linearized, locally incompressible Navier-Stokes equations in the Fourier domain in order to analyse the behaviour of a single sharp-edged perforation of a MPP. Cylindrical (2D axisymmetric) coordinates are applied in order to benefit from the advantage of symmetry in the calculations. Furthermore, we create very small fillets at the perforation edges in order to avoid a numerical singularity. Using the results from different fillet radius values, we extrapolate to the perfect sharp-edge limit case. In order to verify the numerical results, we carry out experiments with MPP samples. Carefully controlling the pressure amplitude, we make sure the measurements are in the linear regime. We observe deviations in the order of 10% in $Z_t$, which is expected to be mainly due to uncertainties in the geometry of the perforations.

Noticing that the acoustic end-corrections depend mainly on Shear number only, new expressions are proposed for resistive and reactive end-corrections, $\alpha$ and $\delta$.

We expect an increase in the impedance of the MPP in the case of a perfect sharp-edge limit. That implies that, the calculated impedance value for the limit case should be larger than the measured value. It is seen that Samples A and B confirm this hypothesis where as this is not true for Sample C.

For the perfect sharp-edge case, it is seen that the resistive and reactive end-corrections are only a function of $Sh$ for the $t_p/d_p$ range investigated $\mathcal{O}(1)$. This means that the numerical results are in accordance with the theory and the controversy in the experimental results for only one sample may have occurred due to the uncertainties in the geometry.

The proposed resistive and reactive end-correction coefficients have limit values for high $Sh$ as suggested by Morse and Ingard[8] for the very thin boundary layer case. Yet, they are not the same. Morse and Ingard proposed that $\alpha = 2$ and $\delta = 1.64$ for the very thin boundary layer (i.e. $Sh >> 1$) case; however, the proposed fits in this study suggest these values to be $\alpha = 1.48$ and $\delta = 1.56$. Since we carry out this study for the range $1 < Sh < 14$, the Shear number might still be too small to represent the acoustic behaviour for the limit investigated by Morse and Ingard. As a result, this affects the asymptotic results of $\alpha$ and $\delta$. Nevertheless, according to Maa[1], the range $1 < Sh < 10$ is very important for a MPP. Therefore, the proposed end-correction coefficients cover this range.

Further work is now needed to determine similar fit formulas for arbitrary edge geometries.

## Acknowledgements

## REFERENCES

1  Maa, D.-Y. Potential of Microperforated Panel Absorber, *J. Acoust. Soc. Am.*, **104** (5), 2861–2866, (1998).

2  Ingard, U. On the Theory and Design of Acoustic Resonators, *J. Acoust. Soc. Am.*, **25** (6), 1037–1061, (1953).

3  Bolton, J. S., Kim, N. Use of CFD to Calculate the Dynamic Resistive End Correction for Microperforated Materials, *Acoustics Australia*, **38** (3), 134–139, (2010).

4  Allam, S., Åbom, M. A New Type of Muffler Based on Microperforated Tubes, *Journal of Vibration and Acoustics*, **113** (031005), 1–8, (2011).

5  Kirchhoff, G. Uber der Einfluss der Wärmeleitung in einem Gase auf die Schallbewegung, *Annalen der Physik and Chemie*, **134** , 177–93, (1868).

6  Peters, M. C. A. M, *Aeroacoustic Sources in Internal Flows*, Doctor of Philosophy Thesis, 167, Eindhoven University of Technology, (1993).

7  Allard, J. F., Atalla, N. 2nd Ed., *Propagation of Sound in Porous Media*, John Wiley & Sons, West Sussex, UK, 45–72, (2009).

8  Morse, P. M., Ingard, U. *Theoretical Acoustics*, McGraw-Hill, New York, USA, 460–463, (1986).

9  Aurégan, Y., Leroux, M. Failures in the Discrete Models for Flow Duct with Perforations: an Experimental Investigation, *Journal of Sound and Vibrations*, **265**, 109–121, (2003).

10  Ingard, U., Ising, H. Acoustic Non-Linearity of an Orifice, *J. Acoust. Soc. Am.*, **42**, 6–17, (1967).